

# Nanoscale

rsc.li/nanoscale



ISSN 2040-3372

**COMMUNICATION**

Takuya Okamoto, Vasudevanpillai Biju *et al.*  
Dual-color photoluminescence modulation of zero-  
dimensional hybrid copper halide microcrystals



Cite this: *Nanoscale*, 2024, **16**, 5107








Received 30th October 2023,

Accepted 2nd January 2024

DOI: 10.1039/d3nr05503e

rsc.li/nanoscale

## Dual-color photoluminescence modulation of zero-dimensional hybrid copper halide microcrystals†

Rahul Ghosh Dastidar, <sup>a</sup> Takuya Okamoto, <sup>\*a,b</sup> Kiyonori Takahashi, <sup>a,b</sup> Yuta Takano, <sup>a,b</sup> Chakkooth Vijayakumar, <sup>c,d</sup> Challapalli Subrahmanyam <sup>e</sup> and Vasudevanpillai Biju <sup>\*a,b,e</sup>

Zero-dimensional hybrid copper(i) halides (HCHs) are attractive due to their interesting photoluminescence (PL) properties and the high abundance and low toxicity of copper. In this study, we report green–red dual emission from rhombic 1-butyl-1-methyl

piperidinium copper bromide [(Bmpip)<sub>2</sub>Cu<sub>2</sub>Br<sub>4</sub>] microcrystals (MCs) prepared on borosilicate glass. The structure and elemental composition of the MCs are characterized by single crystal X-ray diffraction analysis, scanning electron microscopy, and energy-dispersive X-ray spectroscopy. Interestingly, MCs prepared on an ITO-coated glass plate show an intense green emission compared to the dual emission on a bare glass or plastic substrate. Furthermore, the intensity of the green emission from the MC is enormously increased by powdering using a conductive material, suggesting the deactivation of the red-emitting state by a charge transfer interaction with the conductor. These findings open a new strategy to suppress the self-trapping of excitons by longitudinal optical phonons and control the dual emitting states in HCHs.

<sup>a</sup>Graduate School of Environmental Science, Hokkaido University, Sapporo, Hokkaido 060-0810, Japan. E-mail: okamoto@es.hokudai.ac.jp, biju@es.hokudai.ac.jp

<sup>b</sup>Research Institute for Electronic Science, Hokkaido University, Sapporo, Hokkaido, 001-0020 Japan

<sup>c</sup>Chemical Sciences and Technology Division, CSIR-National Institute for Interdisciplinary Science and Technology (NIIST), Thiruvananthapuram 695 019, India

<sup>d</sup>Academy of Scientific and Innovative Research (AcSIR), Ghaziabad 201 002, India

<sup>e</sup>Indian Institute of Technology Hyderabad, Kandi, Telangana 502285, India

† Electronic supplementary information (ESI) available: Table S1 and Fig. S1–S8. Sample preparation schemes, PL images, PL spectra, SEM image, EDX elemental maps, PXRD pattern, photocount maps (PDF), and crystallographic data for (Bmpip)<sub>2</sub>Cu<sub>2</sub>Br<sub>4</sub> (CIF). See DOI: <https://doi.org/10.1039/d3nr05503e>

## Introduction

Organic–inorganic hybrid metal halides have emerged as a new class of photoluminescent materials.<sup>1</sup> Although lead halide perovskites are promising for optoelectronic devices,<sup>2</sup> substitutes are required to replace toxic lead<sup>3,4</sup> and improve stability.<sup>5,6</sup> Pb-free metal halides with various metals (Cu, Sn, Ge, Ag, In, Mn, Sb, Bi, and Ti),<sup>7</sup> organic ligands, and dimensions have been demonstrated recently.<sup>1,8–10</sup> Low-dimensional hybrid copper halides (HCHs) have received much attention owing to the high abundance of copper and their low toxicity.<sup>11</sup> HCHs find applications such as in solar cells,<sup>12</sup> LEDs,<sup>13–15</sup> X-ray scintillators,<sup>16,17</sup> and optical sensors.<sup>18</sup> HCHs show characteristic electronic and optical properties such as flat band edges, wide and tunable bandgaps, large Stokes shifts, and delayed emission. Delayed and broad self-trapped excitonic emission is different from prompt excitonic emission, showing a narrow photoluminescence (PL) band and a short PL lifetime.<sup>1,11,19</sup> Despite these interesting properties of HCHs, the origin of the PL with different spectral maxima and lifetimes and its correlation to the HCH structure and exciton–phonon interactions remain to be unraveled.



**Takuya Okamoto**

*Takuya Okamoto received his Ph. D. degree in molecular materials science from the Graduate School of Science, Osaka City University, Japan, in 2020 under the guidance of Prof. Tomoyuki Yatsushashi. During this period, he was the recipient of the JSPS doctoral fellowship. Subsequently, he was a JSPS postdoctoral fellow with Prof. Biju at Hokkaido University, becoming an assistant professor at the Research Institute for*

*Electronic Science in December 2022. He received the 37<sup>th</sup> Inoue Research Award for Young Scientists in 2020. His research interests are focused on controlling the structure and optical properties of self-assembled lead halide perovskite nanomaterials and hybrid metal halides.*



Due to the  $d^{10}$  configuration of the Cu(I) ion, HCHs form various structures and comprise different compositions.<sup>20</sup> The PL properties of HCHs are controlled by their dimensionality related to the connectivity between the inorganic motifs rather than the crystal morphology or particle size. Several HCH materials have been investigated to correlate the structure, chemical composition, and dimension with optical properties.<sup>8–10,13–18,21–31</sup> For instance, Xu *et al.* synthesized zero-dimensional HCHs, namely 1-butyl-1-methyl piperidinium copper bromide  $[(\text{Bmpip})_2\text{Cu}_2\text{Br}_4]$ , showing a broad orange emission with a large Stokes shift.<sup>17</sup> Peng *et al.* reported three different zero-dimensional HCHs,  $(\text{C}_4\text{H}_9)_4\text{NCuCl}_2$  (508 nm),<sup>21</sup>  $(\text{CH}_3\text{NH}_3)_4\text{Cu}_2\text{Br}_6$  (524 nm),<sup>22</sup> and  $(\text{Gua})_3\text{Cu}_2\text{I}_5$  (481 nm),<sup>23</sup> showing broadband emissions with large Stokes shifts. These optical properties result from self-tapped exciton (STE) states. Also, a few examples of one- and two-dimensional HCHs have been reported.<sup>8,9,11</sup> Several HCHs show dual emission from two different excited states.<sup>24–28</sup> Fu *et al.* reported two hybrid Cu(I) iodides showing broadband emission attributed to triplet and STE states.<sup>24</sup> Lian *et al.* reported dual emission of  $\text{C}_{16}\text{H}_{36}\text{NCuI}_2$  single crystals and correlated the temperature-dependent STE state populations with the thermal activation energy of the STEs.<sup>25</sup> The STE states of tetrabutylammonium (TBA) copper iodides  $[(\text{TBA})_2\text{Cu}_2\text{I}_4]$  are discussed with the electron–phonon coupling and multi-phonon modes.<sup>26,27</sup> Recently, Wang *et al.* demonstrated temperature-dependent dual emission from  $(\text{C}_4\text{H}_{12}\text{N}_2)_2\text{Cu}_2\text{Br}_4$  single crystals.<sup>28</sup> These single crystals show bright blue emission at high temperatures whereas at low temperatures (<100 K) they show two different STE state emissions (460 nm and 605 nm) due to increased lattice distortion. The mechanical modulation of the STE states is also reported.<sup>29,30</sup> Bentio *et al.* found a mechanochromic luminescence of phosphine-based  $[\text{Cu}_4\text{I}_4]$  cluster polymorphic crystals.<sup>29</sup> Wu *et al.* demonstrated multi-stimuli responsive luminescence of  $(\text{CN}_3\text{H}_6)_3\text{Cu}_2\text{I}_5$  crystals.<sup>30</sup> Although modulating the STE emission from HCHs is important for PL band broadening and optical switching, the methods to control it are still limited to those using heat and mechanical force.

Here, we report the modulation of dual-color emission from solution-processed  $(\text{Bmpip})_2\text{Cu}_2\text{Br}_4$  microcrystals (MCs) interacting with an insulating or conducting surface under blue light excitation (*ca.* 400 nm). The optical microscopy images show rhombic MCs with edge lengths of *ca.* 200  $\mu\text{m}$ . Single crystal X-ray diffraction (SCXRD) results suggest that the MCs exhibit an orthorhombic phase.<sup>17</sup> The MCs prepared on a borosilicate glass plate show green (*ca.* 540 nm)–red (*ca.* 620 nm) dual emission under blue light excitation (404–405 nm). Interestingly, the MCs prepared on an ITO-coated glass plate show an intense green emission compared to red emission. Both MCs show similar PL excitation (PLE) spectra and homogeneous distribution of Cu and Br with a stoichiometric ratio of  $\text{Br}/\text{Cu} = 2$ . When broken using a stainless-steel spatula, the MCs prepared on a borosilicate glass plate also showed an intense green emission. Such dual emission and changes to the emission color point towards modification of the electronic structure of the band edge. We discuss the origin of the enhanced green emission from the viewpoint of changes to

the STE states and exciton recombination rates on insulating and conductive materials.

## Experimental

### Materials

1-Butyl-1-methylpiperidinium bromide (BmpipBr,  $\text{C}_{10}\text{H}_{22}\text{BrN}$ , >97%) and copper bromide (CuBr, 98%) were purchased from Tokyo Chemical Industry (TCI). Dehydrated ethanol (99.5%) was purchased from FUJIFILM Wako Chemicals. ITO-coated glass (Ossila, UK) and borosilicate glass (Matsunami) were used as the crystallization substrates. All chemicals were used as received without further purification.

### Preparation of $[(\text{Bmpip})_2\text{Cu}_2\text{Br}_4]$ MCs

We prepared  $(\text{Bmpip})_2\text{Cu}_2\text{Br}_4$  MCs by a modified wet chemistry method<sup>17</sup> (Fig. S1†). Briefly, a precursor solution of  $(\text{Bmpip})_2\text{Cu}_2\text{Br}_4$  was prepared by mixing BmpipBr (472 mg, 2 mmol) and CuBr (144 mg, 1 mmol), and dissolving the mixture in 30 mL of dehydrated ethanol in a two-necked flask. This reaction mixture was heated at 80 °C for 2 h under an Ar atmosphere. After cooling it down to room temperature, 2 mL of the reaction mixture was dropped onto a borosilicate glass plate or an ITO-coated glass plate placed in a Petri dish. Single crystals of  $(\text{Bmpip})_2\text{Cu}_2\text{Br}_4$  were grown at room temperature.

### X-ray structural analysis

The structural analysis of the as-prepared  $(\text{Bmpip})_2\text{Cu}_2\text{Br}_4$  single crystals was performed using a Rigaku XtaLAB-Synergy diffractometer with a HyPix-6000 area detector and multilayer mirror-monochromated Mo kappa radiation ( $\lambda = 0.71073 \text{ \AA}$ ). An MC was mounted on a MicroMounts™ tip (MiTeGen) with Paratone 8277 (Hampton Research). Multiscan absorption corrections were applied to the crystals for the reflection data. The data were processed using the CrysAlisPRO interface (Oxford Diffraction, Agilent Technologies UK Ltd). The simulated XRD pattern was obtained based on the obtained data using the X-ray wavelength (Cu kappa,  $\lambda = 0.15406 \text{ nm}$ ). Also, we recorded the powder XRD (PXRD) patterns of the  $(\text{Bmpip})_2\text{Cu}_2\text{Br}_4$  crystals powdered using a stainless-steel spatula, on an X-ray diffractometer (SmartLab, RIGAKU) with a Cu kappa ( $\lambda = 0.15406 \text{ nm}$ ) X-ray source.

### PLE measurements

PLE spectra of  $(\text{Bmpip})_2\text{Cu}_2\text{Br}_4$  MCs prepared on a borosilicate glass plate and an ITO-coated glass plate were measured using a fluorescence spectrometer (F-4500, Hitachi).

### PL measurements

Optical microscope images, PL images, and PL spectra of samples mounted on an inverted optical microscope (Olympus, IX71) were measured using a digital camera (Olympus, STYLUS XZ-2) and a fiber optic spectrometer (Ocean Optics, FLAME-S). The samples were excited with a 404 nm CW diode laser (Thorlabs, 6.5 mW). The PL from the samples was collected using a  $10\times$  or  $4\times$  Olympus objective lens ( $\text{NA} =$



0.60) and passed through a 480 nm long-pass filter. The sample temperature was controlled and measured using a micro heat plate (KITAZATO, KM-1) and an infrared thermometer (KAIWEETS, Appolo 6), respectively.

### Scanning electron microscope (SEM)–energy dispersive X-ray (EDX) measurements

The topographical images were obtained using SEM (SU8230, Hitachi) operating at an acceleration voltage of 1 kV. EDX mappings were also carried out for those samples using a Bruker SEM-EDX (QUANTAX EDS) operated at 20 kV. The MCs prepared on a borosilicate glass plate were sputter coated with gold for 30 s to avoid charging using a magnetron sputter (MSP-1S, VACUUM DEVICE) with a gold target. The stoichiometry ratio of Br/Cu was calculated from the EDX peaks of Br ( $\kappa\alpha$  line 11.9 keV) and Cu ( $\kappa\alpha$  line 8.0 keV).

### Time-resolved PL measurements

PL photons from samples excited using a femtosecond (fs) laser were detected using a Chromex spectrometer (model 250IS, Chromex) and Streak camera assembly (model C4334, Hamamatsu). The seed NIR fs laser pulses from a mode-locked Ti:Sapphire laser (Coherent Mira 900F, 150 fs, 76 MHz) were amplified using a regenerative amplifier (Coherent RegA 9000, 200 kHz) and converted to second harmonic generation (SHG) pulses (405 nm) by the SHG crystal in an optical parametric amplifier (Coherent OPA 9400). The PL decay curves of the MC prepared on a borosilicate glass plate powdered using a plastic spatula and a stainless-steel spatula were fitted by a biexponential decay model.

## Results and discussion

The (Bmpip)<sub>2</sub>Cu<sub>2</sub>Br<sub>4</sub> MCs synthesized by the simple wet chemistry method are rhombic-shaped (Fig. 1a). The MCs are optically transparent under white light, indicating low absorption in the visible region. The edge length of the MCs ranges from 90 to 400  $\mu\text{m}$  (Fig. 1b). The short reaction time (2 h) and the small sample volume for crystallization (2 mL) enabled the size reduction of the (Bmpip)<sub>2</sub>Cu<sub>2</sub>Br<sub>4</sub> crystals from the mm-scale to the  $\mu\text{m}$ -scale. The crystal structure of the MCs was determined using SCXRD, as shown in Fig. 1c–e. The Cu–Cu bonding of Cu<sub>2</sub>Br<sub>4</sub><sup>2-</sup> in Fig. 1c–e is a pseudo one. The Cu–Cu bond was absent in the SCXRD data (CIF file, ESI†). Details of the crystal structure of the MCs are summarized in Table S1.† The SCXRD data indicate that (Bmpip)<sub>2</sub>Cu<sub>2</sub>Br<sub>4</sub> crystallizes in the orthorhombic space group *Pbca* with crystal parameters  $a = 13.82 \text{ \AA}$ ,  $b = 12.04 \text{ \AA}$  and  $c = 17.08 \text{ \AA}$ ,  $\alpha = \beta = \gamma = 90^\circ$ . The experimental PXRD pattern of the MCs and simulated ones from SCXRD in Fig. 1f match with those in ref. 17.

PL images and spectra of the MCs were obtained by exciting the samples at 404 nm (3.07 eV), which is comparable with the experimental bandgap based on the Tauc plot reported by Xu *et al.*<sup>17</sup> Fig. 2a and b shows the optical transmission image and PL image of (Bmpip)<sub>2</sub>Cu<sub>2</sub>Br<sub>4</sub> MCs prepared on a borosilicate glass plate. The rhombic MCs show green–red dual emission (Fig. 2c) under 404 nm CW laser excitation. The dual emission of the MCs shows two distinct components at *ca.* 541 nm and *ca.* 619 nm. The intensity ratio of these emission peaks depends on the MCs. Some MCs show an intense red emission with a faint yellow emission on the edges (Fig. S2†).

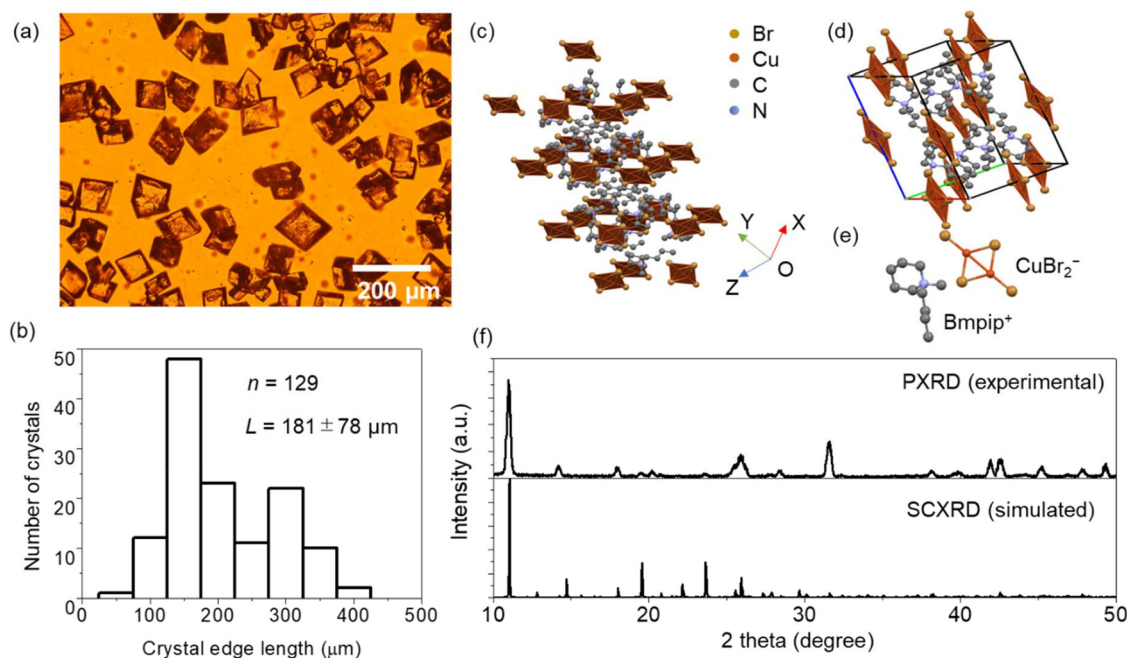


**Fig. 1** (a) An optical microscopy image of (Bmpip)<sub>2</sub>Cu<sub>2</sub>Br<sub>4</sub> MCs. (b) The size distribution of the MCs measured from optical microscopy images.  $n$  and  $L$  denote the number of crystals and mean crystal edge length, respectively. (c) The crystal structure and (d) a unit cell of (Bmpip)<sub>2</sub>Cu<sub>2</sub>Br<sub>4</sub>. (e) The molecular structures of the organic cation Bmpip<sup>+</sup> and inorganic cluster Cu<sub>2</sub>Br<sub>4</sub><sup>2-</sup>. (f) Experimental PXRD and simulated XRD patterns of the MC.



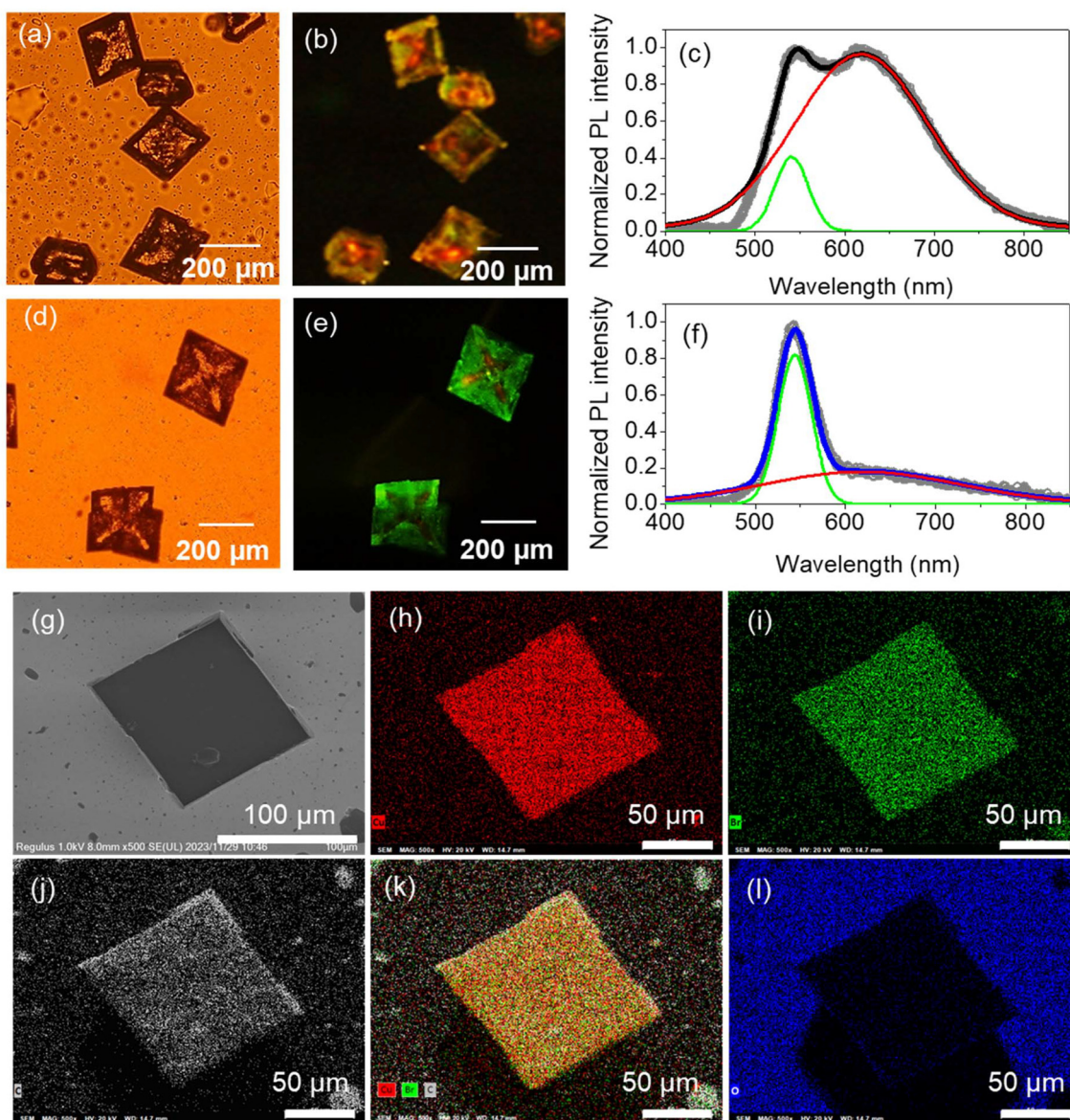
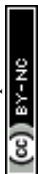


**Fig. 2** (a and d) Optical microscope images, (b and e) PL images, and (c and f) normalized PL spectra of  $(\text{Bmpip})_2\text{Cu}_2\text{Br}_4$  MCs prepared on (a–c) borosilicate glass and (d–f) ITO-coated glass plates. The PL spectra were normalized at 541 nm and fitted by Gaussian functions (black, blue, green, and red lines). The MCs were excited by a 404 nm CW laser. The emitted photons were filtered by a 480 nm long-pass filter. (g) An SEM image, (h–l) EDX elemental maps of (h) copper, (i) bromide, (j) carbon, (k) an overlaid image of copper, bromide, and carbon, and (l) oxygen of the MC prepared on an ITO-coated glass plate.

The yellow color overlays the green and red PL, which are clearly resolved in the PL spectra. Interestingly, the MCs prepared on an ITO-coated glass plate ( $\text{MCs}_{\text{ITO}}$ ) show an intense green emission under 404 nm excitation, as shown in Fig. 2e. The size and shape of  $\text{MCs}_{\text{ITO}}$  are comparable with those of the MCs prepared on the borosilicate glass plate. Inside the  $\text{MCs}_{\text{ITO}}$  shows weak yellow emission. The PL spectrum of the  $\text{MCs}_{\text{ITO}}$  is shown in Fig. 2f, indicating that the red PL contributes to the faint yellow emission inside the crystals. Both MCs and  $\text{MCs}_{\text{ITO}}$  show similar PLE spectra for the green (540 nm) and red emission (600 nm) (Fig. S3†). We prepared MCs on a borosilicate glass plate with a small amount of water

( $\text{MCs}_{\text{water}}$ ) in the precursor solution to confirm whether humidity affects the PL of MCs.<sup>31</sup> We added 10  $\mu\text{L}$  of water to 2 mL of the  $(\text{Bmpip})_2\text{Cu}_2\text{Br}_4$  precursor solution before placing the solution on a borosilicate glass plate for crystallization. However, the  $\text{MCs}_{\text{water}}$  show similar dual emission to the MCs prepared on a borosilicate glass plate rather than  $\text{MCs}_{\text{ITO}}$  (Fig. S4†). The SEM images and EDX elemental mappings of an  $\text{MCs}_{\text{ITO}}$  and an MC prepared on a borosilicate glass are shown in Fig. 2g–l and Fig. S5,† respectively. Both MCs show homogeneous atom distribution of copper (Fig. 2h and S5b†), bromide (Fig. 2i and S5c†), and carbon (Fig. 2j and S5d†). Also, the stoichiometry ratio  $\text{Br}/\text{Cu} = 2$  is calculated for both



MCs from EDX profiles. This indicates the purity of the MCs and the Cu(I) state of copper. Moreover, oxygen atom distributions in both samples (Fig. 2l and S5f†) suggest that the oxidation of Cu is unrelated to the green emission.

We consider different possible origins of the dual and enhanced green emission bands of the MCs: (i) mechanical force-induced PL emission state modification, and (ii) semiconductor–conductive material interaction-induced PL emission state modification. To investigate the origin of the intense green emission of the  $(\text{Bmpip})_2\text{Cu}_2\text{Br}_4$  MCs prepared on an ITO-coated glass plate, we investigated the PL properties of MCs prepared on a borosilicate glass plate after cracking and powdering using a plastic (ABS resin, insulator) or metal spatula (stainless-steel, conductor). Although we transferred the MCs prepared on borosilicate glass and those cracked or powdered using a plastic spatula to an ITO-coated glass plate, the MCs still showed dual emission without intense green emission. Fig. 3 shows PL images and PL spectra of two MCs

during the crystal powdering processes. Initially, both MCs show overlaid green (*ca.* 540 nm) and red (*ca.* 620 nm) dual emission. The PL spectra of the samples were normalized at 620 nm to compare the PL intensity ratios of green/red emission. As shown in Fig. 3a and c, the PL intensity ratio (green/red) and the spectral shape were essentially not affected by breaking using a plastic spatula. We also crushed MCs sandwiched between two borosilicate glass plates by applying mechanical stress. However, the green/red PL intensity ratio did not change. In contrast, as shown in Fig. 3b and d, the PL intensity ratio of the green/red emission increased enormously (*ca.* 7.5 times) by cracking and powdering using a stainless-steel spatula as the corresponding spectral shape changed. With increased MC powdering time, the PL intensity ratio (green/red) also increased (Fig. S6†). The green emission peak of the powdered crystals was similar to that of  $\text{MCs}_{\text{ITO}}$  (*ca.* 541 nm). Although powdering MCs with an insulating material such as a borosilicate glass plate or a plastic spatula does not affect the PL color, spectral shape, or

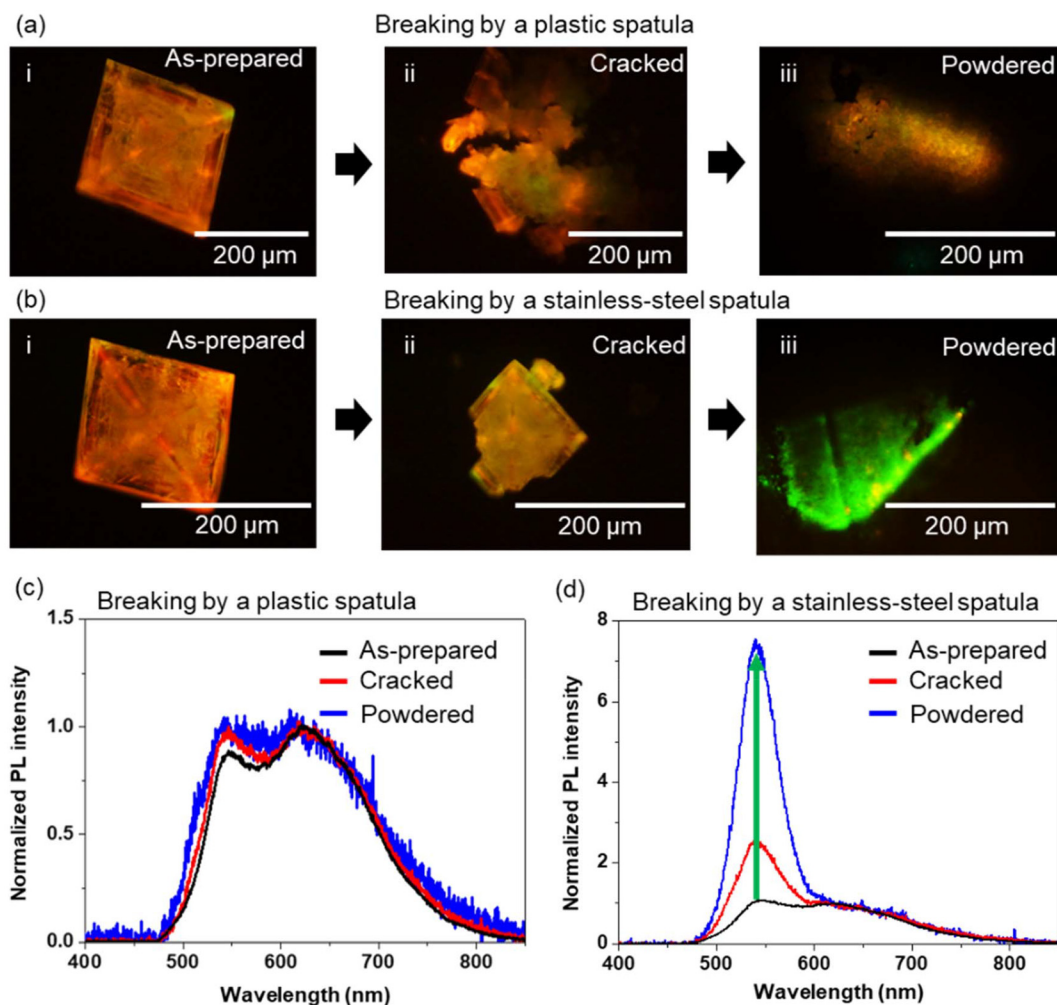


**Fig. 3** (a and b) PL images and (c and d) normalized PL spectra of the (left) as-prepared, (middle) cracked and (right) powdered  $(\text{Bmpip})_2\text{Cu}_2\text{Br}_4$  MCs prepared on borosilicate glass plates. The PL image (iii) in (a) represents a crystal powdered using a plastic spatula. The PL image (iii) in (b) represents a crystal powdered using a stainless-steel spatula. The samples were excited using a 404 nm CW laser. Both PL spectra were normalized at 620 nm. The green arrow indicates the PL spectral change direction.



intensity, we do not rule out the effect of mechanical force on the lattice structure and the energy state of  $(\text{Bmpip})_2\text{Cu}_2\text{Br}_4$ . For example, the mechanical grinding of HCH crystals with a  $\text{Cu}_4\text{I}_4$ <sup>29</sup> or  $\text{Cu}_2\text{I}_5$ <sup>30</sup> core shortens the distance between Cu atoms in those copper cluster cores, lowering the energy of the emitting state. Such a mechanical pressure-induced structural deformation can modify the PL of the MCs. To understand the crystal structure of the samples powdered using a stainless-steel spatula, we measured the PXRD pattern of a powdered sample (Fig. S7†). The PXRD of the powdered sample is well matched with the XRD pattern from SCXRD analysis for the as-prepared MC on a borosilicate glass plate, indicating no phase transition after powdering using a stainless-steel spatula. Slight changes in the diffraction peak intensities and widths of the powder samples are due to the lower crystallinity of powdered crystals than the single crystal. Therefore, the mechanical force negligibly contributes to the modulation of the dual emission states without any phase transition. However, color and PL spectral changes due to the interaction with conductive materials remain an interesting but unsolved issue.

Time-resolved PL measurements help understand the exciton recombination process modulation in  $(\text{Bmpip})_2\text{Cu}_2\text{Br}_4$

Time-resolved PL measurements help understand the exciton recombination process modulation in  $(\text{Bmpip})_2\text{Cu}_2\text{Br}_4$

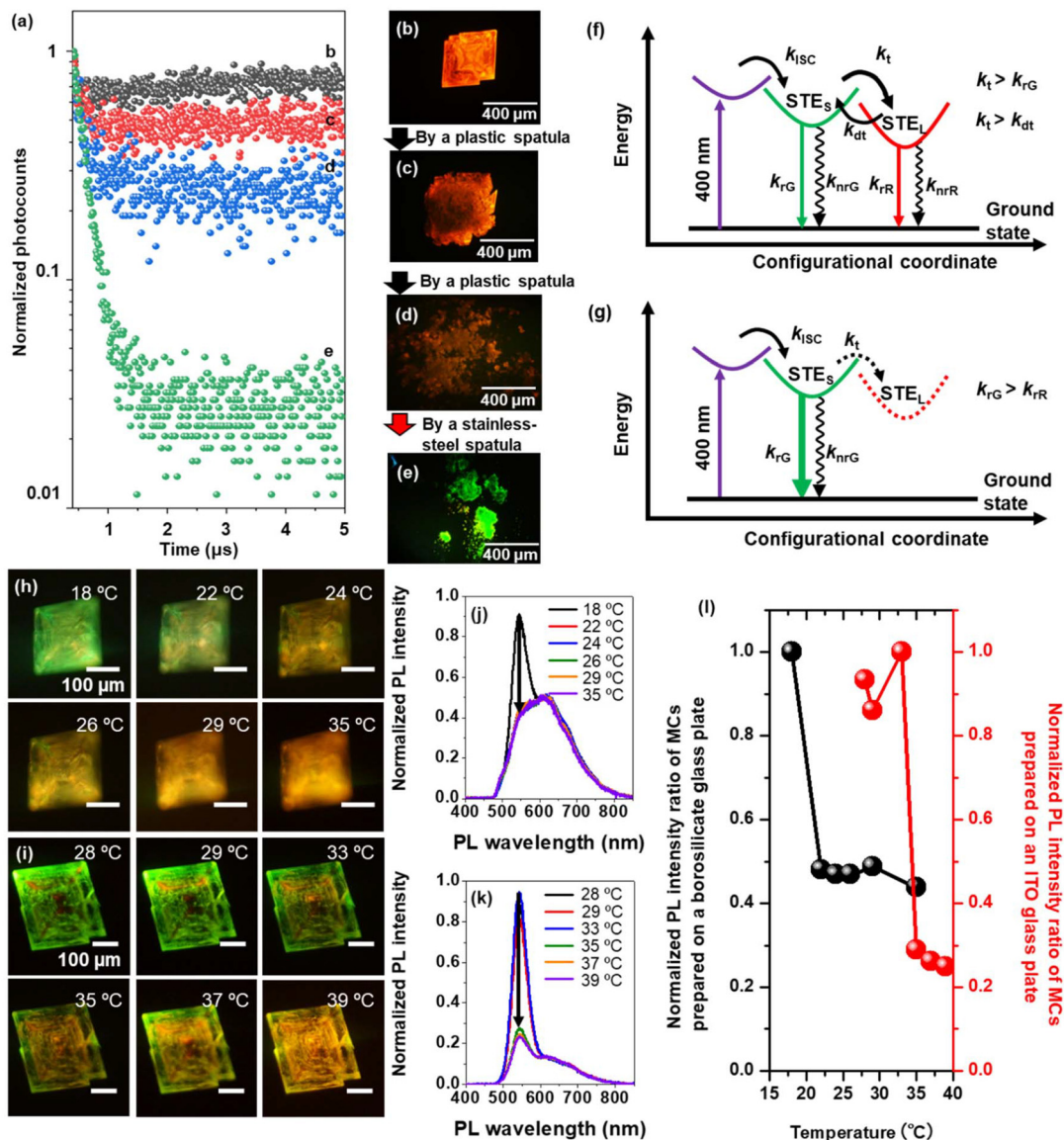


**Fig. 4** (a) PL decay curves and (b–e) PL images of the (b) as-prepared, (c) cracked, and (d and e) powdered  $(\text{Bmpip})_2\text{Cu}_2\text{Br}_4$  MCs. A plastic spatula was used for cracking and powdering in (c) and (d). A stainless-steel spatula was used for powdering in (e). The excitation light source was 405 nm fs laser pulses. (f and g) Schematic diagrams of the STE emission processes of the MCs prepared on a borosilicate glass plate (f) before and (g) after cracking/powdering using a conductive material. (h and i) PL images and (j and k) PL spectra of the  $(\text{Bmpip})_2\text{Cu}_2\text{Br}_4$  MCs prepared on (h and j) borosilicate glass and (i and k) ITO-coated glass plates. Values in PL images (h and i) denote the sample temperature. Both PL spectra were normalized at 612 nm. The samples were excited using a 404 nm CW laser. (l) Temperature dependency of the PL peak intensity ratio ( $I_{543 \text{ nm}}/I_{612 \text{ nm}}$ ) of the  $(\text{Bmpip})_2\text{Cu}_2\text{Br}_4$  MCs prepared on (black) the borosilicate glass plate and (red) the ITO-coated glass plate.



MCs prepared on a borosilicate glass plate during powdering using a plastic or stainless-steel spatula. The samples were excited by fs laser pulses (405 nm, 150 fs, 200 kHz). Fig. 4a shows the PL decay curves of a (Bmpip)<sub>2</sub>Cu<sub>2</sub>Br<sub>4</sub> MC during the powdering process using a plastic spatula (Fig. 4b–d) and a stainless-steel spatula (Fig. 4e). The as-prepared MC (Fig. 4b) shows delayed emission. Fig. 4f shows the exciton recombination process of the MCs prepared on a borosilicate glass plate, showing dual emission.  $k_{rG}$  and  $k_{rR}$  are radiative recombination rates for the green emission and red emission, respectively, and  $k_{nrG}$  and  $k_{nrR}$  are the corresponding non-radiative recombination rates. We attribute the delayed emission to the STE recombination process.<sup>1,17,19</sup> Generally, the STE emission shows a broad spectral width and large Stokes shift.<sup>32</sup> STEs are generated from the lattice distortion induced by exciton (electron) phonon coupling in HCHs. Under photoexcitation, the weakly bound exciton in the highly dielectric MC is quickly self-trapped to the STE state because of the strong electron-phonon interaction. The STEs are easily de-trapped to higher STE states.<sup>19</sup> The strong polaronic effect in the MC retards the electron and phonon. As a result, it can be trapped in a low-lying STE state in high dielectric semiconductors such as (Bmpip)<sub>2</sub>Cu<sub>2</sub>Br<sub>4</sub>. Inter-band relaxation from such an STE state can be further delayed due to repeated trapping–de-trapping processes. The origin of the dual STE states of HCHs is discussed from the viewpoint of exciton–phonon coupling. Peng *et al.* discussed the dual STE states of (TBA)<sub>2</sub>Cu<sub>2</sub>I<sub>4</sub> single crystals based on the multi-phonon mode.<sup>26</sup> A shallow STE state (polaronic state) is formed by the strong electron–phonon coupling (a TBA<sup>+</sup> cation and an I–Cu–I). Two TBA<sup>+</sup> cations and [Cu<sub>2</sub>I<sub>4</sub>]<sup>2-</sup> clusters form a deeper STE state. Although such a model fits with the delayed and red-shifted emission, it cannot explain the dual emission modulation of the MCs induced by mechanical force or the interaction with a conductive material.

We assume that the energy difference between the red and green emission originates due to relaxations from the shallow STE state dominated by the surface phonons and the deeper STE state dominated by the highly polaronic inner lattice phonons. Conversely, the red emission and the green emission of the MCs are assigned to the lattice phonon–exciton-coupled STE state (STE<sub>L</sub>) and the surface–phonon exciton-coupled STE (STE<sub>S</sub>) state, respectively. Based on the surface-to-volume ratio, the density of the lattice phonon is expected to be larger than the surface phonon density in the MCs. Therefore, red emission is dominantly observed in the as-prepared MCs. Here, the STE<sub>S</sub> to STE<sub>L</sub> trapping rate  $k_t$  is greater than the radiative recombination rate from the green emitting STE<sub>S</sub> state ( $k_t > k_{rG}$ ). Also, the trapping rate  $k_t$  is greater than the de-trapping rate ( $k_t > k_{dL}$ ). Therefore, red emission is dominant for the MCs prepared on borosilicate glass plates. To verify those phonon effects on the PL emission color, we conducted temperature-dependent PL measurements for MCs prepared on a borosilicate glass plate or an MC<sub>ITO</sub> (Fig. 4h–l). The MC prepared on the borosilicate glass shows intense green emission at a lower temperature (18 °C) than room temperature (23 °C). The PL emission of the MC changed from green emission to dual

emission with increasing temperature (Fig. 4h). The PL spectra of the MC show resolved dual emission bands as the above-mentioned green–red dual emission peak wavelengths (Fig. 4j). Above the room temperature, the PL peak intensity ratio is constant for the temperature. The MC<sub>ITO</sub> also shows a similar PL emission color change from green emission to dual emission with increasing temperature (Fig. 4i). The PL spectra of the MC<sub>ITO</sub> show a decrease in the PL peak intensity at 543 nm (green emission) with increasing temperature (Fig. 4k). This heat-induced PL color change suggests lattice phonon–exciton-coupling (red emission enhancement). Moreover, the PL emission color differences between MCs prepared on a borosilicate glass plate and an MC<sub>ITO</sub> are due to the temperature threshold differences (Fig. 4l).

After cracking (Fig. 4c) and powdering (Fig. 4d) the MCs with a plastic spatula, the changing trend of peak PL intensity ratio is similar to the result in Fig. 3c (Fig. S8a and b†). The PL decays of these samples show a slight increase in the fast decay component. The fast decay component is associated with the green emission band. Fig. S8d–f† summarizes the fast decay components corresponding to green emission. The narrower bandwidth and faster decay of the green emission compared to the red emission suggest that the green emission state corresponds to the STE<sub>S</sub> state because of the fewer surface phonon–exciton coupling states and lower coupling stability compared to those of lattice phonons. After powdering the MCs, the surface-to-volume ratio is increased but still smaller than the lattice phonon effect due to the micrometer scale crystal size. Therefore, the red and delayed emission is dominant for a sample powdered using an insulating surface. Conversely, the intense green emission after powdering using a conductive surface for the crystal prepared on an ITO-coated glass plate suggests three possible origins of the green emission or de-activation of the red emission: (i) the de-trapping rate from the STE<sub>L</sub> to the STE<sub>S</sub> states exceeds the trapping rates, (ii) the energy of the STE<sub>L</sub> state exceeds the STE<sub>S</sub> state, and (iii) the STE<sub>L</sub> state is deactivated by heat or charge transfer from MCs to ITO or the stainless-steel spatula (Fig. 4f and g). Although an increase in the energy of the lattice–phonon trapped state is unlikely to happen, we do not rule out the other two possibilities, leaving the ultimate solution an open challenge.

## Conclusion

We synthesized zero-dimensional organic–inorganic hybrid copper halide, (Bmpip)<sub>2</sub>Cu<sub>2</sub>Br<sub>4</sub>, rhombic MCs. The MCs prepared on a borosilicate glass plate show green–red dual emission under blue light excitation. Interestingly, the (Bmpip)<sub>2</sub>Cu<sub>2</sub>Br<sub>4</sub> MCs prepared on an ITO-coated glass plate show intense green emission. The MCs also show an intense green emission after powdering using a conductive material. However, the crystals powdered using an insulating material still show red emission. The results of the time-resolved PL measurements and temperature-dependent PL measurements suggest that the red-emitting STE<sub>L</sub> is inactivated by a conduc-





tive material, heat transfer from MCs to conductive materials, or the de-trapping rate from the STE<sub>L</sub> to STE<sub>S</sub> state exceeding the trapping rate when in contact with a conductive surface. These findings open a new strategy for modulation of the dual STE state emissions in HCHs.

## Author contributions

T. O. and V. B. conceived the project. R. G. D. synthesized the MCs. R. G. D., T. O. and V. B. recorded the PL properties of the crystals. R. G. D., T. O., Y. T., C. V., C. S., and V. B. contributed to data analysis. R. G. D., T. O., C. V., C. S., and V. B. contributed to the manuscript. K. T. measured and analyzed the SCXRD. T. O. obtained the PXRD pattern.

## Conflicts of interest

The authors declare that they have no conflict of interest.

## Acknowledgements

This research was supported by JSPS KAKENHI Grant Numbers 21K14580, and 23H01781. We acknowledge the Crossover Alliance to Create the Future with People. R. G. D. acknowledges a JICA Friendship 2 fellowship and V. B. and C. S. acknowledge a JICA Friendship 2 project.

## References

- Z. Wang and X. Huang, *Chem. – Eur. J.*, 2022, **28**, e202200609.
- L. Chouhan, S. Ghimire, C. Subrahmanyam, T. Miyasaka and V. Biju, *Chem. Soc. Rev.*, 2020, **49**, 2869–2885.
- A. Babayigit, A. Ethirajan, M. Muller and B. Conings, *Nat. Mater.*, 2016, **15**, 247–251.
- C. Chen, S. Cheng, L. Cheng, Z. Wang and L. Liao, *Adv. Energy Mater.*, 2023, **13**, 2204144.
- S. Cheng and H. Zhong, *J. Phys. Chem. Lett.*, 2022, **13**, 2281–2290.
- Y. Han, S. Meyer, Y. Dkhissi, K. Weber, J. M. Pringle, U. Bach, L. Spiccia and Y.-B. Cheng, *J. Mater. Chem. A*, 2015, **3**, 8139–8147.
- X. Li, X. Gao, X. Zhang, X. Shen, M. Lu, J. Wu, Z. Shi, V. L. Colvin, J. Hu, X. Bai, W. W. Yu and Y. Zhang, *Adv. Sci.*, 2021, **8**, 2003334.
- L. Zhou, J. Liao and D. Kuang, *Adv. Opt. Mater.*, 2021, **9**, 2100544.
- D. Ma, Y. Lan, D. Zhang, X. Qin, Z. Yang, H. He, X. Dai, Z. Ye and X. Cao, *Mater. Today Chem.*, 2023, **29**, 101408.
- A. Arramel, A. D. Fauzi, X. Yin, C. S. Tang, M. H. Mahyuddin, M. F. Sahdan, M. Aminah, D. Onggo, G. Shukri, C. Diao, *et al.*, *Commun. Mater.*, 2021, **2**, 70.
- D. Banerjee and B. Saparov, *Chem. Mater.*, 2023, **35**, 3364–3385.
- D. M. Fabian, J. W. Ziller, D. Solis-Ibarra and S. Ardo, *ACS Appl. Energy Mater.*, 2019, **2**, 2178–2187.
- Z. Li, Y. Li, P. Liang, T. Zhou, L. Wang and R.-J. Xie, *Chem. Mater.*, 2019, **31**, 9363–9371.
- X. Liu, F. Yuan, C. Zhu, J. Li, X. Lv, G. Xing, Q. Wei, G. Wang, J. Dai, H. Dong, *et al.*, *Nano Energy*, 2022, **91**, 106664.
- X. Liu, Y. Li, L. Zhou, M. Li, Y. Zhou and R. He, *Adv. Opt. Mater.*, 2022, **10**, 2200944.
- P. Mao, Y. Tang, B. Wang, D. Fan and Y. Wang, *ACS Appl. Mater. Interfaces*, 2022, **14**, 22295–22301.
- T. Xu, Y. Li, M. Nikl, R. Kucerkova, Z. Zhou, J. Chen, Y.-Y. Sun, G. Niu, J. Tang, Q. Wang, *et al.*, *ACS Appl. Mater. Interfaces*, 2022, **14**, 14157–14164.
- Y. Wang, S. Zhang, B. Zou and R. Zeng, *J. Phys. Chem. C*, 2023, **127**, 7380–7388.
- Y. Han, X. Cheng and B.-B. Cui, *Mater. Adv.*, 2023, **4**, 355–373.
- X. Hei and J. Li, *Chem. Sci.*, 2021, **12**, 3805–3817.
- H. Peng, X. Wang, Y. Tian, T. Dong, Y. Xiao, T. Huang, Y. Guo, J. Wang and B. Zou, *J. Phys. Chem. Lett.*, 2021, **12**, 6639–6647.
- H. Peng, S. Yao, Y. Guo, R. Zhi, X. Wang, F. Ge, Y. Tian, J. Wang and B. Zou, *J. Phys. Chem. Lett.*, 2020, **11**, 4703–4710.
- H. Peng, X. Wang, Y. Tian, B. Zou, F. Yang, T. Huang, C. Peng, S. Yao, Z. Yu, Q. Yao, *et al.*, *ACS Appl. Mater. Interfaces*, 2021, **13**, 13443–13451.
- P. Fu, S. Geng, R. Mi, R. Wu, G. Zheng, B. Su, Z. Xia, G. Niu, J. Tang and Z. Xiao, *Energy Environ. Mater.*, 2022, e12518.
- L. Lian, P. Zhang, G. Liang, S. Wang, X. Wang, Y. Wang, X. Zhang, J. Gao, D. Zhang, L. Gao, H. Song, R. Chen, X. Lan, W. Liang, G. Niu, J. Tang and J. Zhang, *ACS Appl. Mater. Interfaces*, 2021, **13**, 22749–22756.
- H. Peng, Y. Xiao, Y. Tian, X. Wang, T. Huang, T. Dong, Y. Zhao, J. Wang and B. Zou, *J. Mater. Chem. C*, 2021, **9**, 16014–16021.
- C. W. Meng, C. Wang, Y. Li, G. Hu, S. Sui, G. Xu, M. Peng and Z. Deng, *Chem. – Eur. J.*, 2023, **29**, e202202675.
- Y. Wang, S. Zhang, B. Zou and R. Zeng, *J. Phys. Chem. C*, 2023, **127**, 7380–7388.
- Q. Benito, X. F. Le Goff, S. Maron, A. Fargues, A. Garcia, C. Martineau, F. Taulelle, S. Kahlal, T. Gacoin, J.-P. Boilot and S. Perruchas, *J. Am. Chem. Soc.*, 2014, **136**, 11311–11320.
- J. Wu, Y. Guo, J. Qi, W. Yao, S. Yu, W. Liu and S. Guo, *Angew. Chem., Int. Ed.*, 2023, **62**, e202301937.
- S. Fang, B. Zhou, H. Li, H. Hu, H. Zhong, H. Li and Y. Shi, *Adv. Opt. Mater.*, 2022, **10**, 2200605.
- J. Tan, D. Li, J. Zhu, N. Han, Y. Gong and Y. Zhang, *Nanoscale*, 2022, **14**, 16394–16414.

